Pipe two-phase flow non-invasive imaging using Ultrasound Computed Tomography: A two-dimensional numerical and experimental performance assessment

William Cailly, Henri Walaszek, Sébastien Brzuchacz, Fan Zhang, Philippe Lasaygues

Pipe two-phase flow non-invasive imaging using Ultrasound Computed Tomography: a two-dimensional numerical and experimental performance assessment

William Cailly[a,b,*], Henri Walaszek[a], Sébastien Brzuchacz[a], Fan Zhang[a], Philippe Lasaygues[b]

[a] *Technical Centre for Mechanical Industry, CETIM, France*
[b] *Aix-Marseille Univ, CNRS, Centrale Marseille, LMA, Marseille, France*

Abstract

Pipe two-phase flow non-invasive imaging is of great interest in the field of industry. In particular, small bubble flow imaging through opaque pipes is challenging. Ultrasound computed tomography can be a relevant technique for this purpose. However, perturbation phenomena that are inherent to the configuration (acoustic impedance mismatching, circumferential propagation, reverberation) limit two aspects: the performance of the technique and the use of conventional inversion algorithms. The objectives of the presented work are: (i) to predict the effects of the pipe wall on ultrasonic waves for both metallic and plastic pipe, (ii) to define a consistent inversion algorithm taking into account those effects, (iii) to validate and to assess the limitations of the designed imaging numerical tool using an experimental setup. The benchmark configuration consists of 150 mm diameter 3 mm thick pipes containing 6 mm diameter rods acting as reference scatterers. Two materials of very different acoustical properties were tested: aluminum and PMMA. The results highlighted that the quality of the reconstructed image is very dependent on the pipe material. The results showed that, using an adapted inversion model, consistent target reconstruction is obtained. Based on numerical predictions, performance limitations are reached for metallic pipes.

Keywords: Ultrasound computed tomography, two-phase flow, adjoint tomography

1. Introduction

1.1. Context and purpose

Process monitoring is of great importance in the field of chemical, oil and gas industries. Process tomography regroups imaging techniques that permit the monitoring of industrial processes. Such techniques give information about a state of a process by means of a real-time visualization. In particular, for multiphase flow, the purpose is to

*Corresponding author
Email address: cailly@lma.cnrs-mrs.fr (William Cailly)

know the spatial distribution of the various phases flowing through a pipe from non-invasive measurements. The two-phase flow regime is a steady state depending on the gas concentration and on the relative velocity between the two phases. In particular, the bubbly flow occurs when the flow rate of the liquid is significantly higher than the flow rate of the gas. This bubbly flow regime occurs not only during controlled flow in reactors but also during heterogeneous advected cavitation phenomena. Small voids that are formed on the inner surface of a pipe are advected when there is a liquid flowing through this pipe. Bubbles are moving and different dynamical effects occur : Archimedes' acceleration, expansion and break. Heterogeneous cavitation, when it is strong, implies local structural damage such as erosion. Detecting bubbles in order to prevent damage due to cavitation is of great significance for systems like hydraulic circuits, turbines or pumps.

1.2. Background

Different imaging techniques are currently available for process monitoring : optical imaging, electric tomography, MRI, X-ray tomography, ultrasonic imaging [1]. The design of process tomography systems is subject to the trade-off between : (i) image reconstruction time - (ii) cost of instrumentation - (iii) spatial resolution and (iv) temporal resolution. Another restraining factor to non-invasive process tomography is the penetrating power of waves. Electromagnetic waves are limited to relatively thin and low density walls. Moreover, optical imaging is only applicable to transparent walls and liquids. Ultrasound imaging techniques seem to be a good solution where electromagnetic wave techniques are not applicable. Ultrasound techniques can be used on materials for which X-ray techniques have little penetrating power, typically thick steel walls. So, non-invasive imaging of small bubble flow is challenging. It is known that Electrical Capacitance Tomography is not suitable for detecting small bubbles because of its lack of spatial resolution performance. Ultrasound techniques should be more affordable for industry because of fewer technical constraints, lower cost, and absence of safety restriction compared with X-ray or MRI techniques[2].

It is possible to monitor two-phase flow in a pipe by means of fan-beam ultrasound tomography. The 2D fan-beam tomography can be implemented by electronic scanning, that is, an acquisition sequence of signals emitted by a set of N transducers placed around a section of a pipe. In the case of a two-phase flow, the impedance discontinuity at a gas-liquid interface makes it possible to reconstruct the position of interfaces, whose curvature radius is greater than the wavelength, from ultrasonic echoes, using transmission and/or reflection tomography. In [3, 4, 5, 6, 7, 8, 9], Hoyle's research group and other researchers from the University of Leeds showed the feasibility of real-time fan-beam ultrasound tomography for bubbly flow imaging. In [10, 11, 12, 13, 14, 15], Ruzairi Abdul Rahim's group achieved good results for the application of transmission ultrasound tomography to two-phase flow in bubble column reactors. Recent results have been presented by Langener *et al.* [16]. It is possible to apply time-of-flight difference tomography to reconstruct a quantitative map of the plane components of the velocity field of a liquid flow [17, 18, 19]. A similar tomographic method has been used to the whole 3-component velocity field [20]. Overall, this background shows that the advantages of ultrasound tomography are its low cost, high contrast and good spatial resolution. However, the major limitations of ultrasound techniques are (i) low temporal resolution, (ii) signal complexity due to refraction and multiple diffraction phenomena (iii) significant mismatching at solid–liquid interfaces. Limitation (i) is related to the

speed of sound. The electronic scanning sequence implies that the reconstructed image is computed from signals emitted at different instants. Limitation (ii) has to be taken into account especially for the case of small bubbles. Indeed, the diffraction pattern of a spherical obstacle whose diameter is nearly the wavelength of ultrasound includes side lodes resulting in a complex directivity. Limitation (iii) depends on the material the pipe is made of. Acoustic impedance matching systems involve artificially minimizing the effects of refraction and reflection at the interface between the wall and the liquid to maximize the energy transmitted between these two media. The reflection coefficient at the steel–water interface with normal incidence is around 94 %. The impedance mismatching at the curved interface of the pipe wall causes refraction of an incident plane wave with a convergent effect. Most researchers in the field of process ultrasound tomography conclude that non-invasive imaging of the inside of a steel pipe is made very difficult because of internal specular reflections [21]. Several solutions to minimize these effects have been studied [22, 23] : (i) focused probes (expensive solution); (ii) inserts machined through the wall (invasive); (iii) multi-element probes with different orientations. Cowell showed that solution (iii) can be a solution to minimize the effect of refraction which will be discussed in this paper. Moreover, the Lamb waves generated in the wall disturb the signals transmitted inside the pipe. This disturbance is significant in the case of steel since most of the energy remains trapped in the wall. An increase in the frequency causes a concentration of the ultrasound intensity within the wall. The idea developed by Abbaszadeh is to minimize the disturbance due to the wall waves by selecting the excitation frequency according to the propagation time of the Lamb waves [21].

1.3. Objectives and content

Within this industrial context and background, the objectives of the presented work are: (i) to predict the effects of the pipe wall on ultrasonic waves for both metallic and plastic pipe, (ii) to define a consistent inversion algorithm taking into account those effects, (iii) to validate and to assess the limitations of the designed imaging numerical tool using an experimental setup.

First, the paper deals with the direct problem. The geometric and acoustic aspects of the problem are exposed. Then, the 2D numerical model is presented. Two inversion methods are defined according to the direct model: an adapted filtered back propagation method (AFBP) and an adjoint field tomography method (AFT). The benchmark configuration focuses on a single geometry: 150 mm diameter and 3 mm thickness for aluminum pipes and PMMA pipes, assuming small bubble concentration and small flow velocity. Results are obtained for a set of both numerical and experimental data from this configuration. The presented results analysis consists in measuring the detection, localization and spatial undersampling performance, for 6 rods mm acting as scatterers. The results are discussed in the last section.

2. Methods

2.1. Geometry of the configuration

Let us consider a 2D cross section of a pipe containing liquid and bubbles considered as perfect impenetrable obstacles. The geometry of the configuration showing the chosen parameters is given in figure 1. The pipe wall Ω_S is a homogeneous elastic isotropic

medium. The liquid in the domain Ω_L is an acoustic medium in which the speed of sound is c_0.

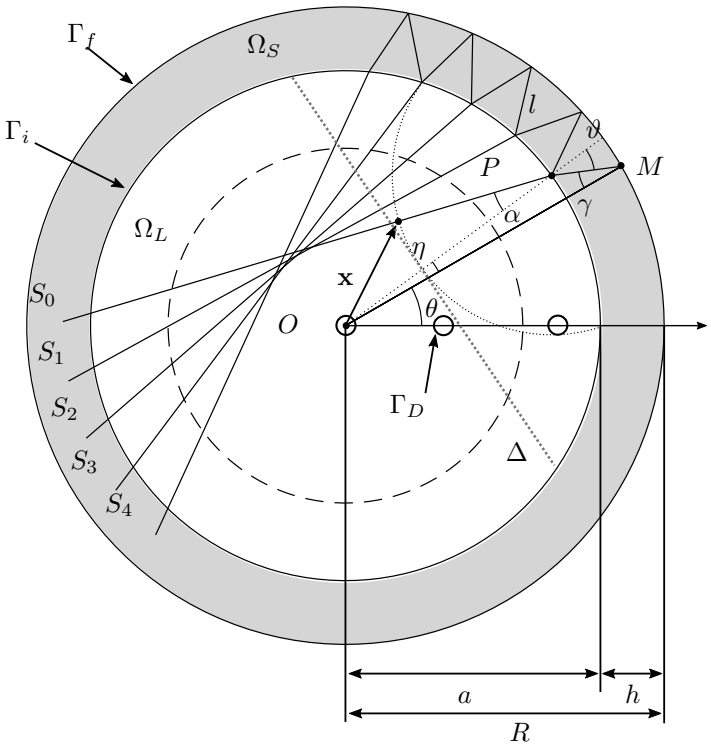

Figure 1: Geometric parameters. The geometry is divided in an acoustic liquid medium Ω_L, and a solid elastic medium Ω_S. Emitter or receiver is located at M. Perfect obstacle surfaces are denoted by Γ_D.

In this study, the chosen pipe diameter $2R$ and thickness h were 150 mm and 3 mm, respectively.

2.2. Acoustic wave transmitted through the pipe

Within the assumption of perfect continuity of pressure and velocity at the interfaces, the transmission transfer function T_t of an infinite elastic layer 1 of thickness h separating a fluid 0 from a fluid 2 is given by

$$T_t(\omega) = t_{01}t_{12}e^{ih\omega/c_L}\left(1 + \frac{r_{10}r_{12}e^{2hi\omega/c_L}}{1 - r_{10}r_{12}e^{2hi\omega/c_L}}\right) \tag{1}$$

Where ω is the angular pulsation, c_L is the pressure wave velocity in the infinite elastic layer, and t_{nm}, r_{rm} are the transmission and reflection coefficients depending on the acoustical impedance of the media (recalled in A.5 and A.6). Similarly, the elastic layer reflection transfer function T_r, relating the incident acoustic field to the reflected acoustic field, is

$$T_r(\omega) = r_{01} + \frac{t_{01}t_{12}}{r_{10}}\frac{r_{10}r_{12}e^{2hi\omega/c_L}}{1 - r_{10}r_{12}e^{2hi\omega/c_L}} \tag{2}$$

These transfer functions, as first approximation neglecting mode conversion and shear waves, are valid for normal incidence and large excitation area compared to the thickness. One can derive the following energy conservation relation

$$T_r T_r^* + T_t T_t^* = 1 \tag{3}$$

The maximum of transmission, corresponding to resonance, occurs at $|T_t| = 1$ when

$$\omega_n = \frac{\pi c_L n}{h} \tag{4}$$

This determines the center frequency for excitation for maximizing the acoustic wave amplitude in the pipe. In this paper, we studied two pipe materials with different acoustical properties: PMMA and aluminum. The transmission transfer function for these materials for $h = 3$ mm are plotted in figure 2. The chosen material constant values are given in table 1.

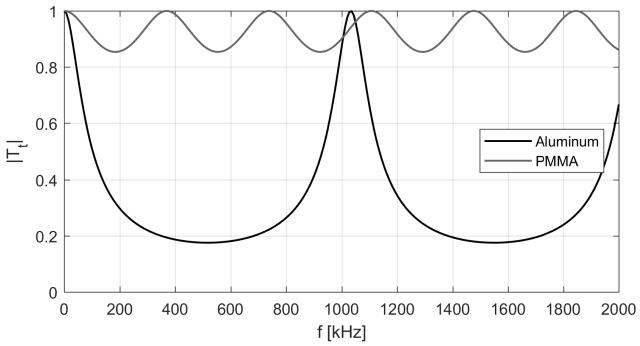

Figure 2: Transmission transfer function of an infinite 3 mm thick layer for PMMA and aluminum.

2.3. Adapted filtered backpropagation ray method

It is possible to use a geometrical optics analogy principles to describe the phenomena caused by the acoustic discontinuity: (i) refraction, (ii) in wall reflections, (iii) interference of leaky waves. Analytical tomography is based on geometric formulation. Under this approximation, a spherical wave can be described as ray paths starting from a point and pointing in all directions. This optics analogy allows to describe reflection, refraction and diffraction according to Snell's law and Huygens' principle. Refraction is only negligible for a small range around the center O. For scatterers close to the wall it is necessary to take into account refraction *i.e.*, ray deviation, due to angular incidence. This approach is valid for small wavelengths compared with the wall thickness, $\omega \gg c_L/h$.

The ultrasonic energy contained in the wall is described as multiple reflected rays. The reverberation and propagation phenomena affect all the sinogram, *i.e.* the measurement at each position around the pipe. The calculated paths are transformed to *phase shift* in order to define a consistent analytical tomography formulation. This formulation describes the phase and amplitude of a wave propagating from a point source within the pipe to the outer surface of the wall. The formulation is equivalent to the diffraction tomography formulation in a homogeneous medium when $c_L \to c_0$ or $h \to 0$. The formulation presented below concerns the passive case (inversion source problem) and can be

easily extended to the active scattering case (emitter–receiver) applying reciprocity and Born approximation. The direct source problem is defined by the following mathematical operation.

$$\mathcal{R} : L^1(\mathbb{R}^2) \to L^1(S^1 \times \mathbb{R}),$$
$$\mathcal{R}f(\theta,\omega) = \int_{-\frac{\pi}{2}}^{\frac{\pi}{2}} t(\gamma) e^{ik_L l(\gamma)} w(\gamma) \sum_{n=0}^{\infty} Q_n(\gamma) d\gamma \tag{5}$$

$$Q_n(\gamma) = |r|^n(\gamma) e^{ink_L 2l(\gamma)} \int_{S_n(\theta,\gamma)} f(\mathbf{x}) H_0^1\left(k_0|\mathbf{x}-\mathbf{x}_n|\right) d\mathbf{x} \tag{6}$$

where f is the contrast function to be reconstructed, H_0^1 is the Hankel function known to be the Green function of the 2D Helmholtz equation in homogeneous medium with $k_0 := \omega/c_0$, S^1 is the unit circle, r and t are the reflection and transmission coefficients oriented from liquid to solid, l is the reflection path. The rays $S_n(\theta,\gamma)$ are defined by a set of geometrical parameters and relations given in appendix. The reconstruction algorithm is the adjoint of the operator including high pass filtering (Filtered Back Propagation, FBP). The far field approximation can be used as in classical diffraction tomography. This approximation reduces the reconstruction computational cost by approximating the curved arrival time locus to tangent lines Δ perpendicular to the direction of observation $\boldsymbol{\theta}$ (see gray dotted line in figure 1). This algorithm is denoted by adapted FBP (AFPB) in the paper.

2.4. The beamforming and circumferential propagation modes

Abbaszadeh *et al.* observed experimentally the effect of circumferential guided waves propagating in a thick steel pipe wall on the signals transmitted to the liquid [21]. The authors observed that a decrease in frequency has the effect of reducing the perturbation caused by circumferential waves. However, to detect scatterers, the decrease in frequency results in a decrease in resolution. Consequently, there exists a trade-off between resolution and transmission of ultrasonic waves in the liquid. The main parameters involved are: (i) tube geometry and material, (ii) excitation frequency, (iii) scatterers global position and size. To deal with the case where the wavelength is close to or greater than the thickness of the wall, it is necessary to go through such wave frequency domain approach. We are particularly interested in the plane-strain circumferential modes with significant radial vibration, which are the equivalents of antisymmetric Lamb plate modes. Indeed, the radial displacement has the effect of transmitting leaky waves in the liquid medium contained in the pipe to be inspected. The analytical approach is described by Gazis, who showed that the modal behavior is determined by the aspect ratio h/R and the Poisson coefficient ν [24, 25]. For the geometry under study $h/R \ll 1$, so the circumferential wave can be approximated to Lamb plate mode.

The ultrasonic beam form, that is, the spatial distribution of transmitted energy, is of great importance for the inspection performance because it determines the resolution and detection power. The shape of the beam inside the pipe is determined by the diffraction occuring at the inner interface. The effect of the wall on the ultrasound beam can be described using the presented geometrical optics formulation. Each reflected wave in the wall transmits a wave whose amplitude depends on the transmission coefficient and

the phase depending on the multiple reflection path. We are interested in the near-field perturbations. It is possible to apply the Huygens' principle to describe the field diffracted by the inner interface.

2.5. Adjoint field computation using a finite element model

Finite difference method (FDM) or finite element method (FEM) can be used to predict complex propagation phenomena. Such methods make it possible to solve direct and inverse problems involving heterogeneous media, in our case liquid-solid media. One of the advantages of FEM compared with FDM is that the positions of the nodes are consistent with the domain boundary geometry, in our case a circle. It also makes the implementation of the boundary conditions easier.

For the FEM model, we supposed that the in-plane components of the liquid flow velocity are negligible. We supposed that the liquid is a homogeneous acoustic medium with bulk modulus κ and density ρ_0. We supposed that the speed of a bubble is much lower than the speed of sound $c_0 = \sqrt{\kappa/\rho_0}$, so that a bubble can be considered as a static obstacle during the ultrasound scanning. The 2D approximation implies that the obstacle is a cylinder. A 3D analysis is required to take into account 3D diffraction due to the spherical shape of a bubble. We considered the following formulation: velocity potential ϕ for liquid, plane strain displacement $\mathbf{u}$ for solid and perfect particular velocity and pressure-traction continuity assumption at the solid-liquid interface Γ_i. The bubbles were considered as Dirichlet obstacles ($\phi = 0$ on Γ_D). The reference phantom consisted in three different radial rod positions: $r_0 = 0$ mm, $r_1 = 24.5$ mm, $r_2 = 48.5$ mm. We used the central difference integration scheme to compute the transient result of the elastic-acoustic dynamic system. We checked the results against those obtained by Komatitsch *et al.* for a flat horizontal interface [26]. A spectral element implementation was used in the cited paper. In our case we chose linear quadrangle and triangle P1 elements. The mass matrix was a lumped-mass matrix, *i.e.*, a diagonal mass matrix approximation. A view of the mesh at the pipe interface is given in figure 3. The average size of the elements was 0.3 mm. The integration step was $\Delta t = 0.02\mu$s.

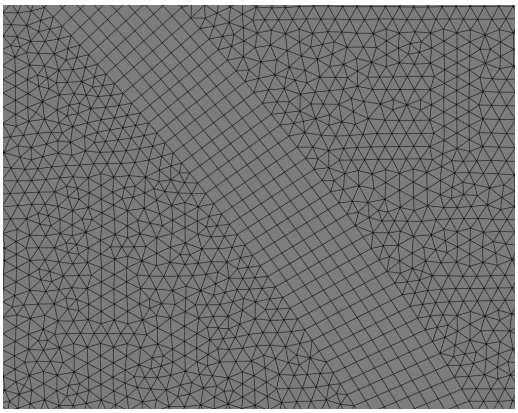

Figure 3: View of the mesh of a 3mm pipe wall with quadrangle elements surrounded by triangle elements.

The problem of recovering consistent scattering information coming from a source perturbed by an aberrating layer is known in acoustics. In the case of a relatively weak impedance discontinuity, the perturbation can be compensated by a phase-shift operation. In our case, severe perturbations, *i.e.*, leaky guided waves and reverberation, due to high impedance contrast, make it difficult to detect the scattering information coming from a point source. Dorme and Fink showed that a physical time-reversal operation on the perturbed signals (having integrated the perturbing layer) makes it possible to focus energy on a point source, and to reconstruct a consistent image [27]. Adjoint field tomography (AFT) consists in computing a time-reversed field to recover the characteristic function of the scatterer. The AFT image is a representation in the space of parameters of the gradient of a functional measuring the error between observed data $\mathbf{d}_{obs}$ and predicted synthetic data $\mathbf{d}_{syn}$, where $\mathbf{d} := [\phi, \mathbf{u}]$ stands for the degrees of freedom vector. The functional χ measuring the error is defined by the following equation

$$\chi(\mathbf{m}) := \frac{1}{2}\int_0^T \int_{\Gamma'_f} (\mathbf{d}_{obs}(\mathbf{x},t) - \mathbf{d}_{syn}(\mathbf{x},t,\mathbf{m}))^2 d\mathbf{x}dt \tag{7}$$

where Γ'_f is a part of the outer surface Γ_f (or a sphere surrounding the object) where the field is measured. The vector $\mathbf{m}$ contains the parameters of the model at each node. The gradient of χ can be expressed in terms of the adjoint field $\mathbf{d}_{adj}$ which is defined by the following equation.

$$L^*\mathbf{d}_{adj} = \mathbf{d}_{obs}(\mathbf{x}',t) - \mathbf{d}_{syn}(\mathbf{x}',t), \mathbf{x}' \in \Gamma_f \tag{8}$$

$$\nabla_{\mathbf{m}}\chi\delta\mathbf{m} = \int_0^T \int_\Omega \mathbf{d}_{adj}(\mathbf{x}, T-t)\nabla_{\mathbf{m}} L\delta\mathbf{m} d\mathbf{x}dt \tag{9}$$

with $\mathbf{x}' \in \Gamma'_f$, and L^* denotes the time-reversal $(T-t)$ of the linear differential operator L associated with the model. The gradient of the functional can be decomposed into sensitivity kernels [28]. The sensitivity kernels take the following time-domain general form.

$$K_{\mathbf{m}}(\mathbf{x}) = \int_0^T \mathbf{d}_{adj}(\mathbf{x}, T-t)\nabla_{\mathbf{m}} L\delta\mathbf{m}dt \tag{10}$$

The domain of interest here is the liquid with parameters (ρ_0, κ). Supposing that the perturbation given by the presence of bubbles is a density perturbation $\delta\rho_0$ (for qualitative representation of the gradient). The associated density kernel for a shot index i takes the following form.

$$K^i_{\rho_0}(\mathbf{x}) = -\int_0^T \dot{\phi}^i_{adj}(\mathbf{x}, T-t)\dot{\phi}^i_{syn}(\mathbf{x},t)\delta\rho_0 dt \tag{11}$$

where $\dot{\phi}$ denotes the time derivative of the velocity potential. A synthetic qualitative image I_{ρ_0}, can be obtained by summing the kernels on shots i, for N shots around the object to inspect.

$$I_{\rho_0}(\mathbf{x}) = \sum_{i=1}^N K^i_{\rho_0}(\mathbf{x}) \tag{12}$$

Parameter	Symbol	Value	unit
Pipe outer diameter	$2R$	150	mm
Pipe thickness	h	3	mm
Speed of sound in liquid	c_0	1480	m/s
Scatterer (rod) diameter	d	6	mm
Reference position of scatterer 1	r_0	0	mm
Reference position of scatterer 2	r_1	24.5	mm
Reference position of scatterer 3	r_2	48.5	mm
Aluminum			
Young modulus	E	70	GPa
Density	ρ	2700	kg/m^3
Poisson ratio	ν	0.33	
Plastic			
Young modulus	E	3.3	GPa
Density	ρ	1190	kg/m^3
Poisson ratio	ν	0.37	

Table 1: Numerical values.

2.6. Experimental setup

The experiments consisted in immersion scanning of pipes. Because beamforming is determined mainly by the diffraction at the inner interface, immersion configuration only affects the way the outer interface is excited. Steel rods 6 mm in diameter acting as pure reflectors were placed in the pipe at the chosen positions r_0, r_1, r_2. Each rod position was measured individually. The diffraction-mode acquisition process was performed using a laboratory ultrasonic immersion system with mechanical scanning. The acquisition consisted in scanning the target in the diffraction tomography mode with 45 shots around the target, giving an emission angular step of 8 degrees. The receiver range was a limited backscattering aperture of 180 degrees divided into 11 positions, giving a reception angular step of 16 degrees. The transducers used were IMASONIC$^{\text{TM}}$ 500 kHz with an active diameter of 42 mm and IMASONIC$^{\text{TM}}$ 250 kHz with an active diameter of 44 mm. The electric excitation pulse was generated by an Olympus-Panametrics$^{\text{TM}}$ pulser-receiver. The signals were digitized and recorded using a Lecroy$^{\text{TM}}$ oscilloscope. The sampling frequency was set at 50 MHz. The transducers were located at 225mm far from the center.

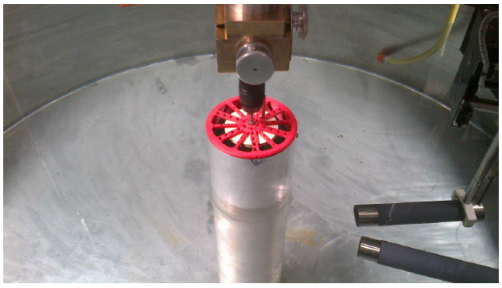

Figure 4: Photograph of the immersion experimental setup.

2.7. Methodology for experiments

For both numerical and experimental testings, three configurations were selected:

- PMMA 3 mm 500 kHz, 3 rod positions
- aluminum 3 mm 500 kHz, 3 rod positions
- aluminum 3 mm 250 kHz, 3 rod positions

The direct ultrasonic field calculations were done according to the experimental setup configuration. The direct ultrasonic beam was computed considering the measured transducer impulse response as the source in the model. For the simulations, adjoint fields were computed for 8 angular positions equally spaced around the pipe. The adjoint source locus consisted of the full aperture divided into 1024 points. For the experimental reconstruction, 9 angular positions equally spaced over 45 were computed. For both adjoint field and adapted FBP, the source location corresponded to the transducer center of aperture. The inversion algorithm were applied to the subtracted signal to the empty pipe (no scatterers) measurements. The inversions were performed on CPU desktop computer.

The image analysis consisted in measuring (i) the consistency of the location of the reconstructed scatterers and (ii) the amplitude of the reconstructed scatterers. The amplitude of each scatterer position allowed to measure the radial amplitude decrease due to undersampling effect near the pipe wall. The rate of decrease was computed using a normalized (value of 1 at $r = 0$) exponential fit f:

$$f(r) = e^{-r/r_c} \tag{13}$$

where r is the radial position and r_c is the parameter of the fit, called the critical radius. The signal-to-noise ratio (SNR) was measured comparing the average amplitude of the scatterers A_s to the average amplitude of inconsistent information on the reconstructed images A_n that included: measurement apparatus electronic noise, circumferential echo perturbation, and reconstruction artifacts. The SNR is given in dB: $20 \log_{10}(A_s/A_n)$. The synthetic accuracy criterion for a given reconstruction was defined by the average absolute error measured taking the difference between reconstructed peak positions and real scatterer positions.

3. Results

The ultrasonic field computations for the three selected configurations are given in figure 5. The fields are given in linear normalized scale relative to the maximum amplitude of excitation from outside the pipe. The AFT simulation results are given in figures 6, 7 and 8. The AFPB experiments results are given in figures 9, 10 and 11. The figures 10a and 10b compare the effect of subtracting the empty pipe acquisition to the measured signals for the same acquisition. The radial cross sections of AFBP for the 3 rod positions for each configuration are given in figures 12, 13 and 14. Cross section normalization is done relatively to the centered scatterer amplitude. On the cross section figures, the real positions of the scatterers are given by vertical dotted lines. AFT experiments results are given in figures 15. Similarly radial cross sections of AFT for the 3 rod positions for the two tested configurations are given in figures 16 and 17. The tomography images are qualitative and are given in linear normalized grayscale. The measurements of critical radius and SNR (defined in the previous section) for all image reconstruction are given in table 2.

3.1. Ultrasonic field: numerical results

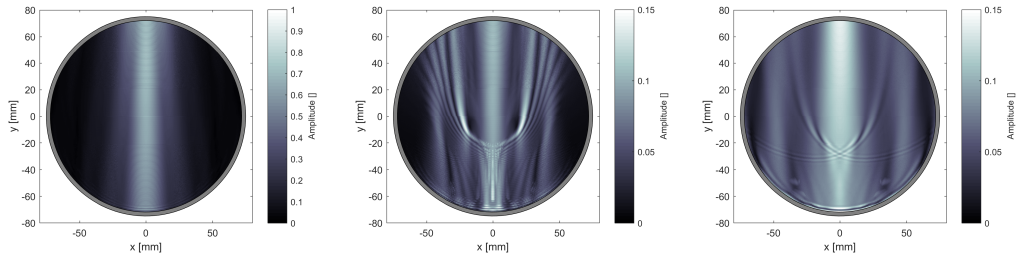

(a) PMMA 3 mm 500 kHz. (b) aluminum 3 mm 500 kHz. (c) aluminum 3 mm 250 kHz.

Figure 5: Numerical computations of ultrasonic field in the pipe, given in linear normalized scale relative to the maximum amplitude.

291 *3.2. Adjoint field tomography: numerical results*

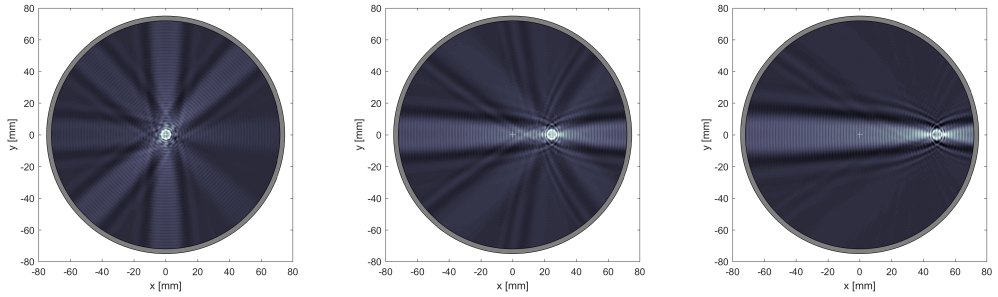

(a) 6 mm diameter rod at position r0.

(b) 6 mm diameter rod at position r1.

(c) 6 mm diameter rod at position r2.

Figure 6: 8 shots adjoint field tomography from simulated data for the PMMA pipe at 500kHz.

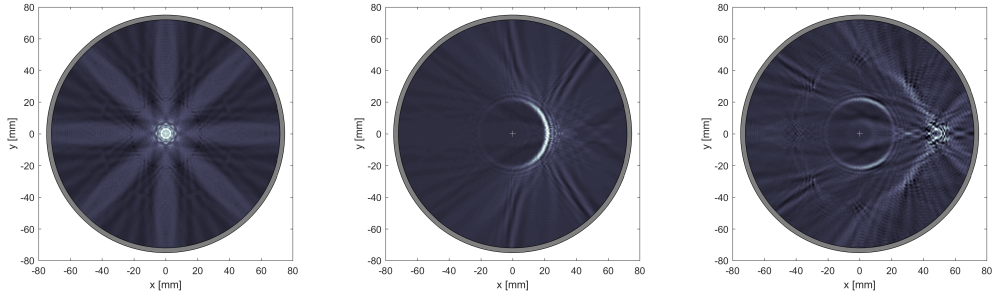

(a) 6 mm diameter rod at position r0.

(b) 6 mm diameter rod at position r1.

(c) 6 mm diameter rod at position r2.

Figure 7: 8 shots adjoint field tomography from simulated data for the aluminum pipe at 500kHz.

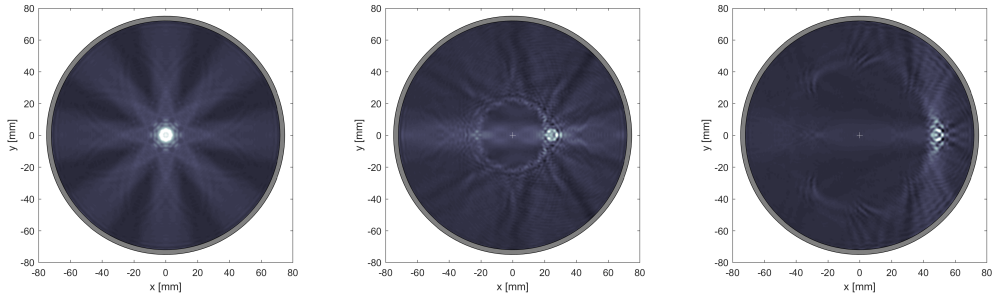

(a) 6 mm diameter rod at position r0.

(b) 6 mm diameter rod at position r1.

(c) 6 mm diameter rod at position r2.

Figure 8: 8 shots adjoint field tomography from simulated data for the aluminum pipe at 250kHz.

3.3. Experimental results

3.3.1. PMMA3mm 500 kHz

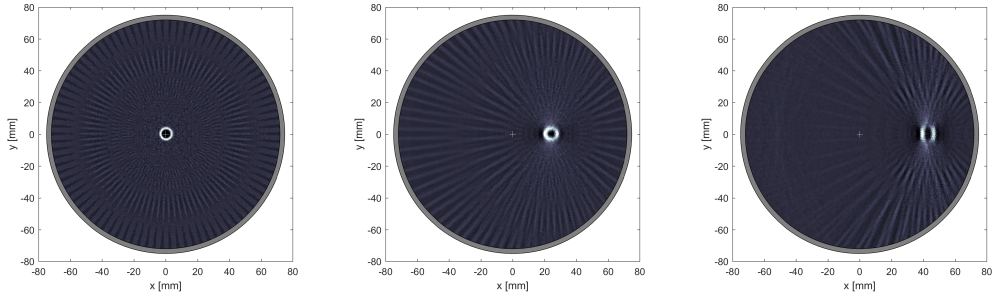

(a) 6 mm diameter rod at position r0.

(b) 6 mm diameter rod at position r1.

(c) 6 mm diameter rod at position r2.

Figure 9: Tomography of PMMA pipe 3 mm 500 kHz, with adapted FPB.

3.3.2. ALU 3 mm 500 kHz

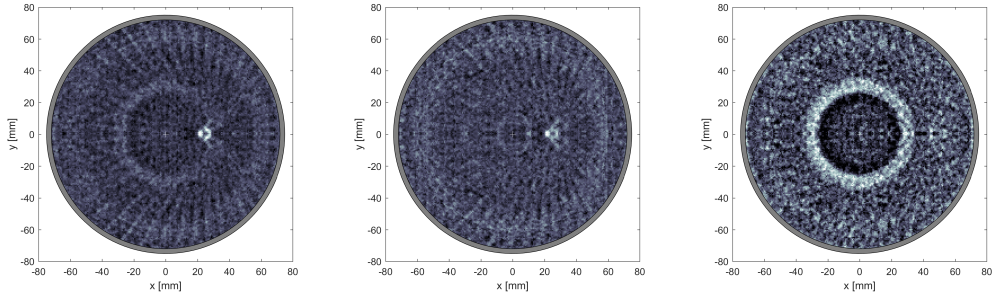

(a) 6 mm diameter rod at position r2 without subtraction of empty pipe reference signals.

(b) 6 mm diameter rod at position r2 with subtraction of empty pipe reference signals.

(c) 6 mm diameter rod at position r3 without subtraction of empty pipe reference signals.

Figure 10: Tomography of aluminum 3 mm pipe, 500 kHz, with adapted FPB.

3.3.3. ALU 3 mm 250 kHz

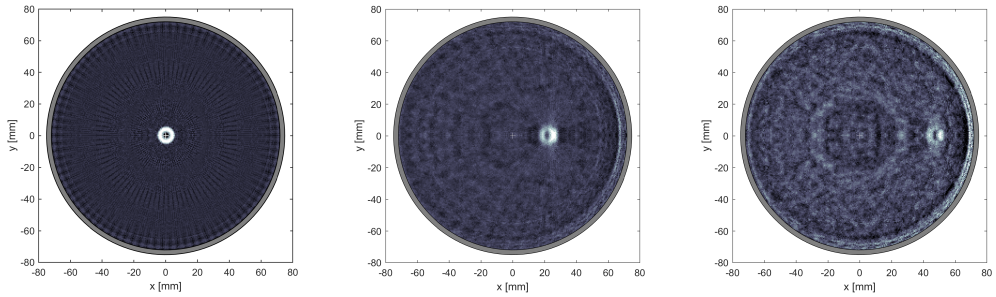

(a) 6 mm diameter rod at position r0.

(b) 6 mm diameter rod at position r1.

(c) 6 mm diameter rod at position r2.

Figure 11: Tomography of aluminum pipe 3 mm 250 kHz, with adapted FPB.

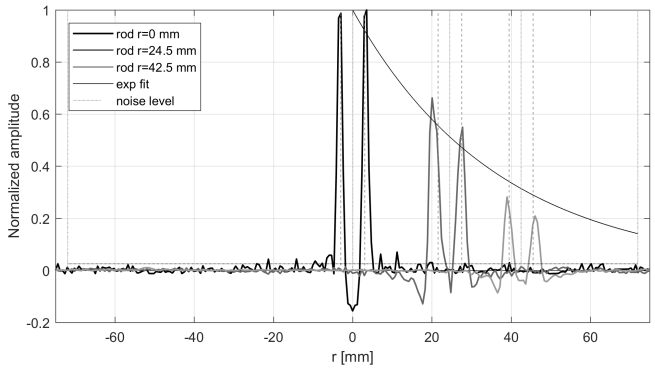

Figure 12: Radial cross section of PMMA 3 mm 500 kHz tomography for the 3 rod positions.

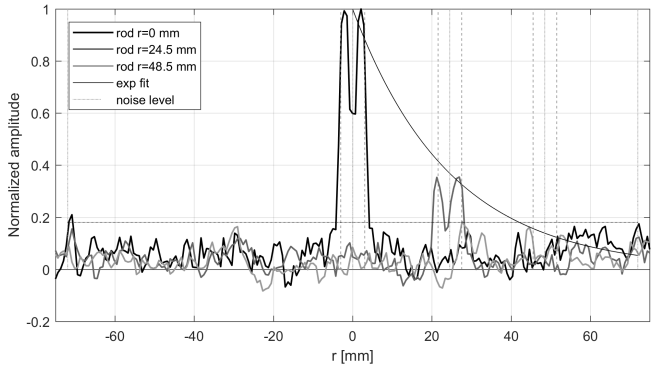

Figure 13: Radial cross section of aluminum 3 mm 500 kHz tomography for the 3 rod positions.

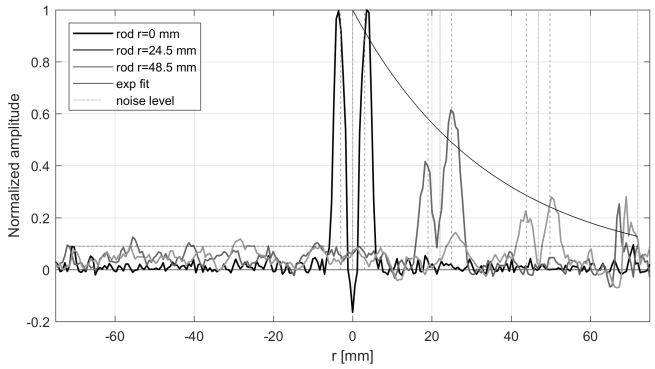

Figure 14: Radial cross section of aluminum 3 mm 250 kHz tomography for the 3 rod positions.

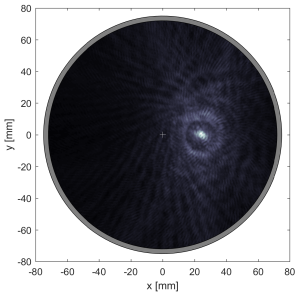

(a) PMMA 3 mm 500 kHz, 6 mm diameter rod at position r1.

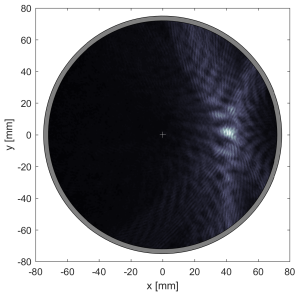

(b) PMMA 3 mm 500 kHz, 6 mm diameter rod at position r2.

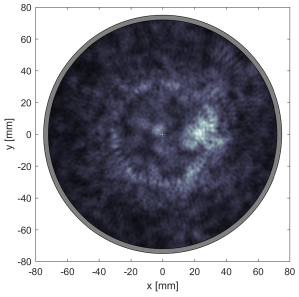

(c) aluminum 3 mm 250 kHz, 6 mm diameter rod at position r1.

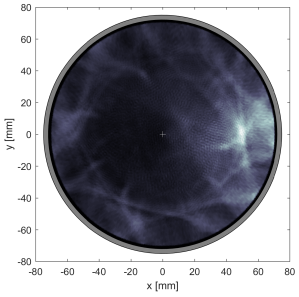

(d) aluminum 3 mm 250 kHz, 6 mm diameter rod at position r2.

Figure 15: Adjoint field tomography results for different configurations, 9 shots.

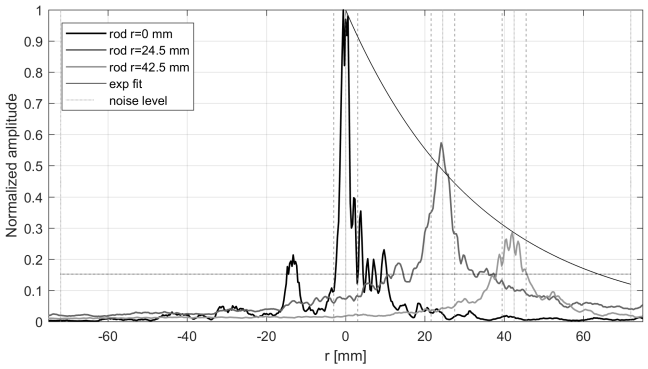

Figure 16: Radial cross section of AFT PMMA 3 mm 500 kHz tomography for the 3 rod positions.

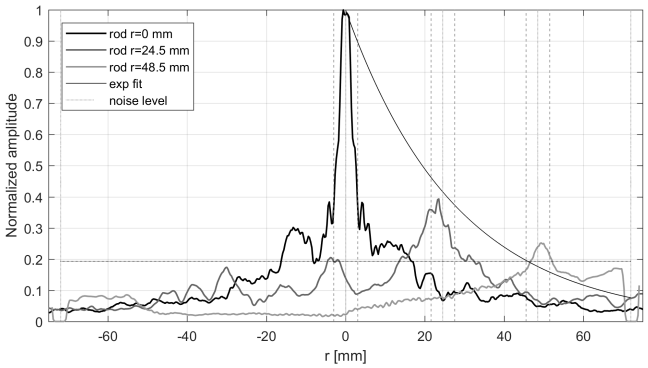

Figure 17: Radial cross section of AFT aluminum 3 mm 250 kHz tomography for the 3 rod positions.

3.3.4. Summary of results

Configuration	r_c (mm)	SNR	avg abs err (mm)
Simulation PMMA 3 mm 500 kHz	40.4	24.2 dB	0.21
Simulation aluminum 3 mm 500 kHz	25.7	17.3 dB	0.27
Simulation aluminum 3 mm 250 kHz	39.5	19.7 dB	0.23
Experiment PMMA 3 mm 500 kHz	36.7	32.0 dB	0.56
Experiment aluminum 3 mm 500 kHz	24.6	14.9 dB	0.58
Experiment aluminum 3 mm 250 kHz	36.0	20.9 dB	0.58
Experiment AFT PMMA 3 mm 500 kHz	33.9	16.4 dB	0.27
Experiment AFT aluminum 3 mm 250 kHz	28.0	14.3 dB	0.63

Table 2: Summary of results for all the configurations.

4. Discussion

The results of selected experiments allow to study the influence of (i) the impedance mismatch due to the pipe wall and (ii) the radial position of scatterers on the detection and on the resolution. The configurations are supposed to be valid for relatively small scatterer concentration. As expected, good results are obtained for the PMMA pipe wall. Using the adapted FBP algorithm, it possible to localize the scatterers with good accuracy, see figure 9. On the contrary, artifacts and low detection due to beam perturbation is observed for the aluminum pipe wall. The direct ultrasonic field computations highlight the beam perturbation. The beam remains unperturbed in the case of plastic, contrary to the aluminum case. As can be seen in figures 5b and 5c, the perturbation is not only an amplitude decrease, but also a narrowing effect and interferences. The adjoint field method makes it possible to take into account the actual beam in the liquid. The simulation results make it possible to compare ideal reconstruction to assess the limitations of the method. Concerning the aluminum case, For both simulations and experiments, the results show a ring artifact on the reconstruction that is due to the retropropagation of a circumferential echo. The reconstructed images after subtraction of reference signals (see 10b) show that it is possible to filter this echo. However, it increases the noise level. Due to blinding effect, a dead zone in which the echoes amplitude coming from scatterers are too low, the farthest scatterer from the center, for the aluminum 500 kHz case, is not detected, see figure 10c. Indeed, as shown in the cross section in figure 13 the farthest scatterer amplitude is below the noise level. As predicted by simulation results, better detection is obtained using 250 kHz transducers, see figure 11. For the 250 kHz case, the wavelength is about 6 mm, which is the diameter of the targets. The adjoint field tomography results allow to compare the previous results with an other reconstruction method. The goal is to minimize the number of adjoint field computation. Simulation results with full aperture show that using only 8 shots, consistent scatterer localization is obtained. However, severe artifacts are obtained in the case of aluminum pipe. Reconstructions from experimental data, with limited aperture, show a good localization of the scatterers computing only 9 adjoint fields, see figure 15. Increasing the number of adjoint field computation will increase the contrast, but the computational cost will be higher. The detection and contrast performance can be assessed using the two chosen synthetic quantity: critical radius and SNR. The performance of experimental results are consistent with the simulation results.

5. Conclusion

In this paper we showed that, even for ideal cases the ultrasound computed tomography for bubble flow imaging has some limitations: spatial undersampling, reconstruction artifacts, blinding effect, and lack of information. The quality of non-invasive imaging through a pipe is strongly dependent on the material the pipe is made of. The ultrasonic beam is perturbed by the inherent acoustical impedance mismatch at the inner pipe interface. This limits the performance of the reconstruction. Consequently, images suffer presence of artifact, noise, low SNR. The 500 kHz configuration on the aluminum pipe demonstrates the limitations of the method to detect bubble near the pipe wall. However, in the case of aluminum, we showed that selecting a lower frequency increases the detection and the contrast. The finite-element adjoint approach can be applied with

reasonable computational cost. An adapted FBP algorithm makes it possible to perform consistent and accurate reconstruction of scatterers acting as bubbles through a pipe. Using this reconstruction technique, relatively high-quality images, with consistent target localization and contour reconstruction, can be achieved for plastic pipes.

References

[1] R.A. Williams. Introduction, an overview of process applications of tomographic techniques. In Mi Wang, editor, *Industrial Tomography*, Woodhead Publishing Series in Electronic and Optical Materials, pages xix – xxvii. Woodhead Publishing, 2015.

[2] Christian Poelma. Ultrasound Imaging Velocimetry: a review. *Experiments in Fluids*, 58(1):3, December 2016, doi:10.1007/s00348-016-2283-9.

[3] B. S. Hoyle. Real-time ultrasound process tomography in pipelines. In *IEE Colloquium on Ultrasound in the Process Industry*, pages 1/4–4/4, September 1993.

[4] F. Wiegand and B. S. Hoyle. Development and implementation of real-time ultrasound process tomography using a transputer network. *Parallel Computing*, 17(6):791 – 807, 1991, doi:https://doi.org/10.1016/S0167-8191(05)80067-5.

[5] M. Yang, H. I. Schlaberg, B. S. Hoyle, M. S. Beck, and C. Lenn. Parallel Image Reconstruction in Real-Time Ultrasound Process Tomography for Two-phased Flow Measurements. *Real-Time Imaging*, 3(4):295 – 303, 1997, doi:https://doi.org/10.1006/rtim.1997.0082.

[6] Ming Yang, H. I. Schlaberg, B. S. Hoyle, M. S. Beck, and C. Lenn. Real-time ultrasound process tomography for two-phase flow imaging using a reduced number of transducers. *IEEE Transactions on Ultrasonics, Ferroelectrics, and Frequency Control*, 46(3):492–501, May 1999, doi:10.1109/58.764834.

[7] H. I. Schlaberg, F.J.W. Podd, and B S. Hoyle. Ultrasound process tomography system for hydrocyclones. *Ultrasonics*, 38:813–6, 2000, doi:https://doi.org/10.1016/S0041-624X(99)00189-4.

[8] B.S. Hoyle, X. Jia, F.J.W. Podd, H.I. Schlaberg, H.S. Tan, M. Wang, R. West, R. Williams, and T. York. Design and Application of a Multi-modal Process Tomography System. *Measurement Science and Technology*, 12:1157, 2001, doi:10.1088/0957-0233/12/8/324.

[9] H. I. Schlaberg, M. Yang, B. S. Hoyle, M. S. Beck, and C. Lenn. Wide-angle transducers for real-time ultrasonic process tomography imaging applications. *Ultrasonics*, 35(3):213 – 221, 1997, doi:https://doi.org/10.1016/S0041-624X(97)00002-4.

[10] R. Abdul Rahim, M. H. Fazalul Rahiman, N. Wei Nyap, and K. S. Chan. Monitoring liquid/gas flow using ultrasonic tomography. *Jurnal Teknologi*, 40:77–88, 06 2004, doi:10.11113/jt.v40.417.

[11] R. Abdul Rahim, M. H. Fazalul Rahiman, and M. N. Mohd Taib. Non-invasive ultrasonic tomography: Liquid/gas flow visualization. In *2005 1st International Conference on Computers, Communications, Signal Processing with Special Track on Biomedical Engineering*, pages 243–247, November 2005.

[12] M. H. Fazalul Rahiman, R. Abdul Rahim, and Z. Zakaria. Design and modelling of ultrasonic tomography for two-component high-acoustic impedance mixture. *Sensors and Actuators A: Physical*, 147:409–414, 2008, doi:https://doi.org/10.1016/j.sna.2008.05.024.

[13] M. H. Fazalul Rahiman, R. Abdul Rahim, M. H. Fazalul Rahiman, and M. Tajjudin. Ultrasonic Transmission-Mode Tomography Imaging for Liquid/Gas Two-Phase Flow. *IEEE Sensors Journal*, 6(6):1706–1715, December 2006, doi:10.1109/JSEN.2006.884549.

[14] M. H. Fazalul Rahiman, R. Abdul Rahim, H. Abdul Rahim, Siti Zarina Mohd.Muji, and E.J. Mohamad. Ultrasonic tomography - image reconstruction algorithms. *International Journal of Innovative Computing, Information and Control*, 8:527–538, 2012.

[15] M. H. F. Rahiman, R. A. Rahim, H. A. Rahim, R. G. Green, Z. Zakaria, E. J. Mohamad, and S. Z. M. Muji. An evaluation of single plane ultrasonic tomography sensor to reconstruct three-dimensional profiles in chemical bubble column. *Sensors and Actuators A: Physical*, 246:18 – 27, 2016, doi:https://doi.org/10.1016/j.sna.2016.04.058.

[16] S. Langener, M. Vogt, H. Ermert, and T. Musch. A real-time ultrasound process tomography system using a reflection-mode reconstruction technique. *Flow Measurement and Instrumentation*, 53:107 – 115, 2017, doi:https://doi.org/10.1016/j.flowmeasinst.2016.05.001.

[17] W. M. D. Wright and I. J. O'Sullivan. Ultrasonic Tomographic Imaging of Air Flow in Pipes Using an Electrostatic Transducer Array. *AIP Conference Proceedings*, 657(1):666–673, 2003, doi:10.1063/1.1570200.

[18] Yu. V. Pyl'nov, S. Koshelyuk, P. Pernod, and Yu. I. Kutlubaeva. Ultrasonic tomographic reconstruction of liquid flows using phase-conjugate waves. *Physics of Wave Phenomena*, 20, 2012, doi:https://doi.org/10.3103/S1541308X12030119.
[19] Yu. V. Pyl'nov, L. M. Krutyansky, Yu. I. Kutlubaeva, F. Zoueshtiagh, P. Chainais, V. Herman, and P. Pernod. Ultrasonic Tomography of Nonmixing Fluid Flows. *Physics of Wave Phenomena*, 23:273–278, 2015, doi:10.3103/S1541308X15040056.
[20] N. Besic, G. Vasile, A. Anghel, T. I. Petrut, C. Ioana, S. Stankovic, A. Girard, and G. dUrso. Zernike ultrasonic tomography for fluid velocity imaging based on pipeline intrusive time-of-flight measurements. *IEEE Transactions on Ultrasonics, Ferroelectrics, and Frequency Control*, 61(11):1846–1855, November 2014, doi:10.1109/TUFFC.2014.006515.
[21] J. Abbaszadeh, H. Abdul Rahim, R. Abdul Rahim, S. Sarafi, M. Nor Ayob, and M. Faramarzi. Design procedure of ultrasonic tomography system with steel pipe conveyor. *Sensors and Actuators A: Physical*, 203:215 – 224, 2013, doi:https://doi.org/10.1016/j.sna.2013.08.020.
[22] D. M. J. Cowell, P. R. Smith, and S. Freear. Tomographic array design for online, non-invasive, non-intrusive measurement of magnox slurry during nuclear decommissioning. In *2013 IEEE International Ultrasonics Symposium (IUS)*, pages 1865–1868, July 2013.
[23] W. Kolbe, B. T. Turko, and B Leskovar. Fast Ultrasonic Imaging in a Liquid Filled Pipe. *Nuclear Science, IEEE Transactions on*, 33:715 – 722, 1986, doi:10.1109/TNS.1986.4337200.
[24] D. C. Gazis. Exact analysis of the plane-strain vibrations of thick-walled hollow cylinders. *Journal of The Acoustical Society of America*, 30, 08 1958, doi:10.1121/1.1909761.
[25] D. C. Gazis. Three-dimensional investigation of the propagation of waves in hollow circular cylinders. i. analytical foundation. *Journal of The Acoustical Society of America*, 31, 05 1959, doi:10.1121/1.1907753.
[26] D. Komatitsch, C. Barnes, and J. Tromp. Wave propagation near a fluid-solid interface: a spectral element approach. *Geophysics*, 65:623–631, 08 2000, doi:10.1190/1.1444758.
[27] C. Dorme and M. Fink. Matched filter imaging through inhomogeneous media. In Piero Tortoli and Leonardo Masotti, editors, *Acoustical Imaging*, pages 1–8. Springer US, Boston, MA, 1996.
[28] Jeroen Tromp, Carl Tape, and Qinya Liu. Seismic tomography, adjoint methods, time reversal and banana-doughnut kernels. *Geophysical Journal International*, 160(1):195–216, doi:10.1111/j.1365-246X.2004.02453.x.

Appendix A. Geometrical definitions and relations

The matrices $\mathbf{R}$ are rotation matrices associated to a subscripted angle. The geometric locus $S_n(\theta, \gamma)$ is a ray belonging to the medium Ω_L and obeying the Snell's law for an oblique incident ray making an angle γ with the normal of the circle of center O at the position $a\boldsymbol{\theta}$.

$$\mathbf{x}_n = \mathbf{R}_{2\eta}^n \mathbf{R}_\eta a\boldsymbol{\theta} \tag{A.1}$$

$$\boldsymbol{\theta} := [\cos\theta, \sin\theta]^T \tag{A.2}$$

The Snell's law at the interface $r = a$ is expressed by

$$\frac{\sin\alpha}{\sin\vartheta} = \frac{c_0}{c_L} \tag{A.3}$$

The ray unit direction vector director is

$$\boldsymbol{v} = -\mathbf{R}_\alpha \frac{\mathbf{x}_n}{a} \tag{A.4}$$

The acoustic Fresnel coefficients are

$$r_{12} = \frac{z_2 \cos\vartheta - z_1 \cos\alpha}{z_2 \cos\vartheta + z_1 \cos\alpha} \tag{A.5}$$

$$t_{12} = \frac{2z_1 \cos\alpha}{z_2 \cos\vartheta + z_1 \cos\alpha} \tag{A.6}$$

$$z_i := \rho_i c_i \tag{A.7}$$

The in wall propagation length l corresponds to the length of PM and is expressed by

$$l(\gamma) = \sqrt{h(h+2a) + a^2 \cos^2\vartheta} - a\cos\vartheta \tag{A.8}$$

Geometric relations are given by the following equations.

$$\sin\alpha(\gamma) = \frac{R+d}{R}\frac{c_0}{c_1}\sin\gamma \tag{A.9}$$

$$\cos\vartheta = \sqrt{1 - \frac{\sin^2\gamma(a+h)^2}{a^2}} \tag{A.10}$$

$$\sin\eta = \frac{l(\gamma)}{a}\sin\gamma \tag{A.11}$$

The distance of a refracted ray S_n to the center O is $a\sin\alpha$. The 1D filter along this variable distance is obtained by a ramp filter of the projections weighted by the factor $\frac{a+h}{a}\frac{c_0}{c_L}$, which tends to 1 when $c_L \to c_0, h \to 0$.